Small Animal Imaging with Magnetic Resonance Microscopy

Bastiaan Driehuys, John Nouls, Alexandra Badea, Elizabeth Bucholz, Ketan Ghaghada, Alexandra Petiet, and Laurence W. Hedlund

Abstract

Small animal magnetic resonance microscopy (MRM) has evolved significantly from testing the boundaries of imaging physics to its expanding use today as a tool in noninvasive biomedical investigations. MRM now increasingly provides functional information about living animals, with images of the beating heart, breathing lung, and functioning brain. Unlike clinical MRI, where the focus is on diagnosis, MRM is used to reveal fundamental biology or to noninvasively measure subtle changes in the structure or function of organs during disease progression or in response to experimental therapies. High-resolution anatomical imaging reveals increasingly exquisite detail in healthy animals and subtle architectural aberrations that occur in genetically altered models. Resolution of 100 μm in all dimensions is now routinely attained in living animals, and $(10\ \mu m)^3$ is feasible in fixed specimens. Such images almost rival conventional histology while allowing the object to be viewed interactively in any plane. In this review we describe the state of the art in MRM for scientists who may be unfamiliar with this modality but who want to apply its capabilities to their research. We include a brief review of MR concepts and methods of animal handling and support, before covering a range of MRM applications—including the heart, lung, and brain—and the emerging field of MR histology. The ability of MRM to provide a detailed functional and anatomical picture in rats and mice, and to track this picture over time, makes it a promising platform with broad applications in biomedical research.

Key Words: disease model; magnetic resonance imaging; microscopy; mouse; rat; rodent

Introduction

Small animal imaging, both in vivo and ex vivo, has become increasingly important in biomedical, genetic, toxicologic, and pharmacologic research. The ability to spatially localize morphologic and functional changes in the organ systems of small animals has fostered a better understanding of embryonic development, genetic mutations, potential therapeutic treatments, and the effects of environmental insults. In addition, the capacity to perform repeated noninvasive imaging in the same animal enables us to study the longitudinal progression of a disease or treatment. The importance of small animal imaging is also apparent in the increasing number of commercial imaging systems now available for most modalities.

It became evident in the early 1980s, when magnetic resonance imaging (MRI[1]) started being used clinically, that it offered a rich contrast capable of displaying many physical characteristics of soft tissues. Because of this advantage of MRI compared to x-rays (in which the contrast relies solely on differences in tissue density), there have been considerable efforts to adapt clinical MRI for small animal studies.

The extension of MRI to magnetic resonance microscopy (MRM[1]), however, has not been straightforward. It required a tenfold increase in image resolution in all three dimensions, resulting in signal reductions of at least a factor of 1,000. Overcoming this deficit required the development of technology specific to MRM—magnets, imaging coils, image acquisition sequences, and biological support for small animals in high magnetic fields.

Relative to clinical MRI, small animal MRM poses many additional challenges. An animal in the bore of a physically large and strong magnet is no longer directly accessible to the investigator and thus requires remote physiologic monitoring and delivery of agents. In addition, the strong magnetic field restricts the use of certain types of equipment, particularly those that contain ferrous materials or motors. Furthermore, the radiofrequency pulses and gradients used for imaging distort electrical recordings such as those for cardiac monitoring. These problems are also characteristic of clinical MRI, but are exacerbated in small animal MRM by the large gradients and small bores of the

Bastiaan Driehuys, PhD, is an assistant professor; Alexandra Badea, PhD, and Ketan Ghaghada, PhD, are research associates; and Laurence W. Hedlund, PhD, is a professor, all in the Department of Radiology at Duke University Medical Center in Durham, North Carolina. John Nouls, MS, Elizabeth Bucholz, BS, and Alexandra Petiet, MS, are PhD candidates in the Department of Biomedical Engineering at Duke University. All work was performed at the Duke University Center for In Vivo Microscopy.

Address correspondence and reprint requests to Dr. Bastiaan Driehuys, Center for In Vivo Microscopy, Box 3302, Duke University Medical Center, Durham, NC 27710 or email driehuys@orion.duhs.duke.edu.

[1]Abbreviations used in this article: FOV, field of view; HP, hyperpolarized; MRI, magnetic resonance imaging; MRM, magnetic resonance microscopy; RF, radiofrequency; SNR, signal-to-noise ratio; T, tesla

animal scanners. A further issue is the need to control biological motion, including that of the heart and lung, to avoid pronounced artifacts. Finally, the costs to purchase and maintain MR scanners far exceed those of most other imaging systems.

However, the unique and exceptionally valuable information that can be derived from MRM makes it well worth the investment. The tissue contrast and spatial resolution now attainable by MRM are unrivaled by other modalities and, because MRM is inherently digital and can be 3-dimensional (3D), it is possible to view images of whole animals or organs in virtually any plane. Researchers can perform functional studies with the aid of physiologically controlled imaging sequences that can be synchronized with the injection or inhalation of contrast agents, or with the desired phase of the cardiac cycle. Not least, the ability to use MRM to noninvasively study a single animal over a prolonged course of disease development and treatment can eliminate the need to sacrifice animals, thereby reducing the number of animals needed.

The intent of this article is to provide a basic overview of MRM, how it works, how it is used for small animal imaging, and its broad range of applications for preclinical studies. The examples we provide are drawn primarily from our own laboratory and are by no means exhaustive, nor do they represent the excellent science being pursued in other imaging laboratories. We wish to give the reader an understanding of the capabilities of MRM and what components are necessary to extract the maximum value from this modality. We include suitable references throughout the text to ensure that interested readers can learn about the field in greater detail.

Overview of Magnetic Resonance Imaging

To appreciate the opportunities and limitations of MRM, a basic introduction to the fundamentals of magnetic resonance imaging is useful (Bushberg et al. 2001; Haacke et al. 1999; Hornak 2006). First, it is important to understand MRI's signal source, which originates from the tiny nuclear magnetic moments of the constituent atoms and molecules that make up the object to be imaged. The most commonly detected nuclei, including some that are not native but can be administered, are ^{1}H, ^{3}He, ^{13}C, ^{17}O, ^{19}F, ^{23}Na, ^{31}P, and ^{129}Xe. The proton ^{1}H is the nucleus used for anatomical imaging because of its abundance in tissues (slightly less than the 110 mol/liter concentration in pure water) and large magnetic moment. The other nuclei are useful for functional and metabolic imaging in a wide range of applications; in particular, we discuss ^{3}He and ^{129}Xe below.

The MR scanner that detects and spatially localizes these nuclei consists of several major components. A powerful static magnetic field (B_0) is used to align the nuclei and determine their detection frequency. A radiofrequency (RF[1]) coil surrounding the sample elicits and receives the nuclear magnetic signal. Gradient coils encode the spatial distribution of the nuclei. Finally, a computer synchronizes the application of RF pulses, switching of gradients, reading and digitization of signal, image reconstruction, and image display.

The first step of an MR scan is to place the sample in a magnetic field B_0, which provides an axis for the nuclei to align along or against. In addition to providing an alignment axis, B_0 also causes the nuclei to precess around it (to envision precession, think of a spinning top, its axis tilted slightly away from the vertical axis and tracing an orbit around it). Precession occurs at a precise frequency that is determined by the size of the nuclear magnetic moment and the intensity of B_0: 63 MHz for protons at 1.5 tesla (T[1]) and 500 MHz for protons at 11.7 T, one of the highest magnetic fields commonly available.

Although all nuclei of a certain isotope precess at the same frequency, they do not do so in the same direction. If they are aligned with B_0 they precess in one direction, and if aligned against B_0 they precess in the opposite direction. These counterrotating nuclei cancel one another's signals unless there are more going in one direction than the other. Fortunately, it is slightly more energetically favorable for nuclei to align with B_0 rather than against it, and this population imbalance is called nuclear polarization. It is typically just a few parts per million in even the strongest magnetic fields, and this lack of cooperation among nuclei is one reason MRI is less sensitive than some other imaging modalities. (A new class of imaging agents, hyperpolarized materials, overcomes this problem, as we discuss below.) Collectively, the polarization, density, and strength of the nuclear magnetic moments constitute the nuclear magnetization, which is the signal source in MRI.

The magnetization that forms along B_0 is called longitudinal magnetization, and to be detected its orientation must become transverse to B_0, at which point the changing flux that results from its precession induces a voltage in the surrounding RF coil (in keeping with Faraday's law). The RF coil converts longitudinal into transverse magnetization through the application of electromagnetic energy to the nuclei by means of an RF pulse. For the pulse to affect the nuclei, its frequency must closely match their precession frequency and this close match creates the resonance in MRI.

The transverse magnetization, along with its associated signal, does not persist indefinitely: it decays exponentially with a time constant T_2 determined by the physical and chemical attributes of the particular tissue. For example, the T_2 of the liver at 1.5 T is 40 milliseconds, whereas the T_2 of fat exceeds 60 milliseconds. These T_2 differences can be used to distinguish the tissues by waiting a suitable delay time (called the echo time, or TE) before recording the signal. To image a liver, TE can be set to 30 milliseconds, at which time the liver signal will have decayed whereas the fat signal will remain intense. Such contrast exploiting differences in transverse relaxation is called T_2 weighting and is illustrated in Figure 1A.

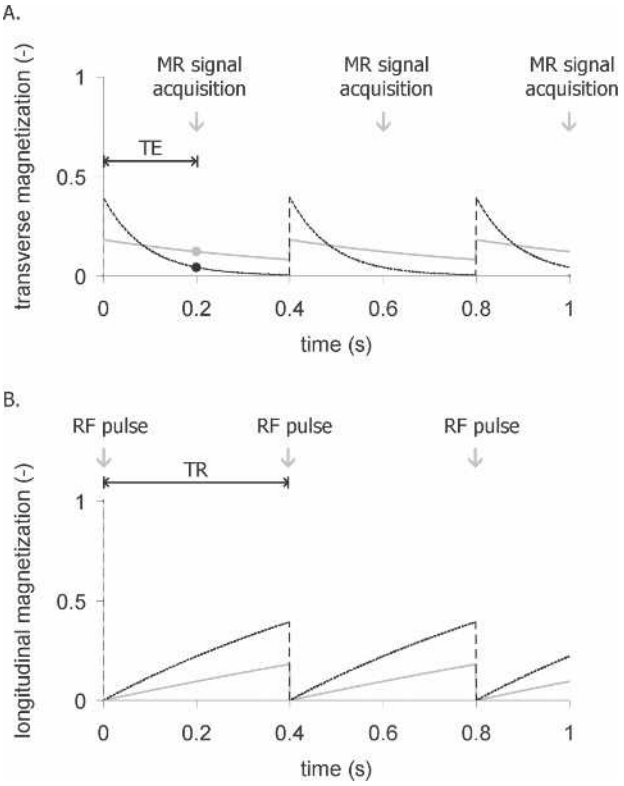

Figure 1 Repetition time (TR) and echo time (TE) can differentiate tissues depending on their T_1 and T_2 values. (A) A 90° radiofrequency (RF) pulse converts the longitudinal magnetization into transverse magnetization to generate an imaging signal. The signal acquisition is delayed by TE to distinguish tissues with different T_2 values. In this example, a tissue with short T_2 (dashed black line) diminishes quickly before the signal is recorded (black dot), while the tissue with a long T_2 (solid gray) retains more signal (gray dot). (B) The RF excitation occurs every TR, creating transverse magnetization (signal) but depleting longitudinal magnetization, which recovers with exponential time constant T_1. In this example, white matter with T_1 = 0.8 s (dashed black) recovers more quickly than cerebrospinal fluid with T_1 = 2 s (solid gray).

To turn the magnetic resonance signal and contrast into an image, the spatial variation of the transverse magnetization must be captured. This is done by exploiting the linear dependence of the nuclear resonance frequency on magnetic field strength. Applying a magnetic field that varies linearly as a function of position (a gradient) disperses the resonance frequencies across the sample. The frequency dependence of the signal acquired in the presence of a linear gradient describes the spatial variation of the sample in one dimension. The image is then built up into two and three dimensions by acquiring many such signals, while encoding gradients are applied in three orthogonal directions to capture the full structure of the object. Image acquisition thus requires many repeated RF excitations and signal readouts to fully encode the 3D structure of a sample line by line. For example, assembling a 3D image resolved into 256 × 256 × 256 pixels requires 256^2 RF excitations to acquire 256^2 image lines of 256 points each, a process that can take considerable time.

The repeated application of RF pulses introduces careful timing considerations that also affect image contrast—specifically, the pulse repetition time (TR) and flip angle. For example, a 90° flip angle rotates all the longitudinal magnetization into the transverse plane and generates the largest possible signal, but leaves no magnetization along B_0 for the next pulse. A smaller flip angle pulse produces less transverse magnetization but leaves more longitudinal magnetization for the next pulse. If a very large flip angle is used (e.g., 60° to 90°) then the next pulse must be delayed long enough for magnetization to grow back by longitudinal relaxation. This regrowth is characterized by the exponential recovery time constant T_1, which, like T_2, is also dependent on the physical and chemical attributes of tissues. For example, at a magnetic field of 1.5 T, the T_1 of cerebrospinal fluid (CSF) is ~2 seconds, whereas the T_1 of white matter in the brain is only 0.8 seconds. By applying 90° pulses at short TR intervals (~1 s), magnetization in the CSF will not recover fully, whereas white matter magnetization will largely recover and be brighter in the image. Such contrast exploiting differences in longitudinal relaxation is called T_1 weighting and is illustrated in Figure 1B.

Finally, to provide the lexicon necessary to interpret the magnetic resonance literature, we define a few additional parameters. A typical report might describe image acquisition as follows: FOV = 10 cm, matrix = 128 × 256, slice = 5 mm, bandwidth = 62 kHz, flip angle = 30°, TR/TE = 100/5 ms. Field of view (FOV^1) represents the linear dimension of the square viewing area. The matrix tells us how many pixels are used to sample the FOV (resolution). Slice determines the resolution in the direction orthogonal to the image viewing plane. The bandwidth determines how many pixels per second are acquired and is usually set to strike a balance between image noise and acquisition speed.

The Challenge of MR Microscopy

The foregoing introduction to magnetic resonance lays the groundwork to appreciate the challenges of MR microscopy. One of the most important aspects of any imaging modality is the signal-to-noise ratio (SNR^1). It is readily apparent that the signal decreases as the 3D pixel volume (voxel) decreases, as illustrated in Figure 2, which depicts the striking difference in scale between a human brain and that of a mouse. For the mouse image to retain the same relative anatomical definition as the human image it must be acquired with a voxel volume approximately 3,000 times smaller than that of a human and the accompanying signal loss must be "won back."

One method for increasing signal is to work at higher B_0, which increases the signal frequency and thus the signal voltage induced in the coil. Increasing B_0 also improves signal by increasing the degree of nuclear polarization.

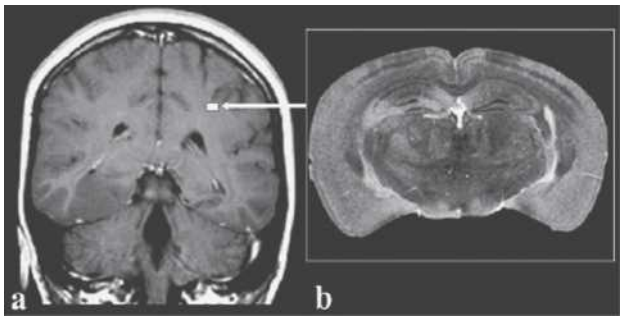

Figure 2 Comparison of (a) a clinical MR image of a 5-mm thick slice of human brain imaged at 1×1 mm^2 in-plane resolution, and (b) a 40-μm thick slice of a mouse brain imaged at 40×40 μm^2 resolution. The size of the mouse brain relative to the human brain is depicted by the white square (arrow). The voxels in the mouse brain image represent a volume 80,000 times smaller than those in the human brain image. Reprinted with permission from Maronpot RR, Sills RC, Johnson GA. 2004. Applications of magnetic resonance microscopy. Toxicol Pathol 32:42-48.

Thus, imaging at 7 T versus 1.5 T can theoretically win back as much as a factor of 5 to 15 in SNR, depending on sample size and on the dominant noise contribution. (The issue of SNR gain versus field strength is somewhat complex, and often SNR gains predicted theoretically are not realized experimentally; see Beuf et al. 2006.) However, the two most important ways to overcome the signal deficits of MRM are by optimizing the RF coil design and by employing longer image acquisition times. Extending imaging times introduces the need for precise physiological control to prevent biologic motion from causing image artifacts.

Microscopic MR imaging also requires renewed attention to the gradient system. The gradients needed to create sufficient resonance frequency dispersion to resolve the pixels across a 4-cm mouse FOV are 10 times larger than those required to resolve the pixels in a 40-cm human FOV. It is therefore not possible to perform MRM on a clinical scanner by simply typing in the desired resolution. A dedicated MR microscope is necessary, with the strong and rapidly switching gradient systems needed to attain high resolution.

Imaging Coils

Perhaps the most critical determinant of imaging performance is the radiofrequency coil (Doty et al. 2007), which drives both signal excitation and reception. Good coils can yield significant signal gains when they are designed to be as small as possible while still covering the anatomical region of interest. Because the coil's sensitivity increases as its volume decreases, reducing coil dimensions from human sizes to rodent sizes can improve SNR by a factor of 20. The coil of choice for most live whole body imaging of rats and mice is the birdcage coil (Figure 3; Hayes et al. 1985). Further reductions in coil size can yield additional sensitivity gains; for example, there are dedicated head coils for brain imaging, and surface coils for cardiac imaging. Coil dimensions can be reduced to extremes, as shown by Summers and colleagues (1995), who implanted an inductively coupled 5-mm diameter coil around the carotid artery of a rat to visualize the development of stenosis.

Figure 3 A 250-g rat prepared for imaging in a 2-T system using a 6-cm diameter birdcage coil. The animal is lying on a Plexiglas cradle and is anesthetized with isoflurane delivered by mechanical ventilation. The hoses to the left are for ventilation gases and the black cables carry signals from ECG electrodes on the foot pads, airway pressure transducer on the breathing valve attached to the endotracheal tube, and body temperature from a thermistor in the rectum. The lower cable connects the coil to the MR scanner.

It is also possible to assemble multiple, high-sensitivity surface coils into larger phased arrays (Gareis et al. 2007), which can deliver high SNR over large regions of interest such as the spine (Beck and Blackband 2001). Alternatively, phased array technology can accelerate imaging speed, although this is less common in MRM than in clinical MRI.

Another advantage of MRM versus clinical MRI is that, up to moderate frequencies (200 MHz), the image noise is largely a function of the electrical noise of the coil rather than noise created by the sample (Black et al. 1993; Edelstein et al. 1986). The noise contributed by the coil corresponds directly to its resistive energy dissipation, which is characterized by its quality factor (Q). A high Q means the coil dissipates little energy and contributes little noise. Q values are generally higher for MRM than for clinical MRI (300 vs. 50), and the higher values translate into another SNR gain by a factor of 2 or 3. Further gains in Q can be attained by cooling the coils to cryogenic temperatures, and such coils are becoming available commercially (Bruker Biospin, Billerica, MA). In fact, extreme gains in Q are possible by using superconducting materials (Darrasse and Ginefri 2003); we discuss this area of research below.

MR Contrast Agents

Beyond the technical factors and imaging physics, another valuable tool for enhancing image quality and organ delineation in MRI is the use of contrast agents. Such agents can further accentuate tissue differences by altering the T_1 and T_2 relaxation times of protons in their vicinity. For example, in a 3-T field, the T_1 of protons in blood falls from about 1,600 to 300 milliseconds after administering a typical bolus of contrast agent. This T_1 reduction highlights the blood vessels when images are acquired using a large flip angle and short TR (T_1-weighted). The majority of T_1-reducing contrast agents are based on the paramagnetic Gadolinium ion, whose large magnetic moment results from its seven unpaired electrons (Caravan et al. 1999). The Gadolinium ion must be chelated because it is toxic in the ionic form and is typically administered at a concentration of 0.1 mmol per kilogram of body weight to substantially alter contrast.

Contrast agent development has progressed tremendously over the years with novel formulations and applications in vascular and molecular imaging (Querol and Bogdanov 2006; Weissleder and Mahmood 2001). The intravenous administration of contrast agents can improve small animal MRM by highlighting vascular changes or delineating tumors. An MRM-specific application of contrast media is to include them in solutions used to fix and "stain" entire specimens for high-resolution imaging.

Fixed-Specimen Preparation and Imaging

While imaging the live small animal is undoubtedly one of MRM's most valuable capabilities, there is also considerable utility in the imaging of fixed specimens, which we discuss here. The use of perfusion-fixation methods employing contrast media was introduced by Johnson and colleagues (2002a,b). These methods increase the achievable anatomic image resolution of MRM from ~$(100\ \mu m)^3$ to $(20\ \mu m)^3$, allowing organs to be studied in superb detail. MRM of perfusion-fixed specimens rivals conventional microscopy because it is nondestructive, can be 3D, and is inherently digital. Furthermore, because the specimens do not have to be dehydrated, as is the case for many conventional histological processes, MRM images show the natural distribution of water in tissues and organs. MRM of specimens achieves the highest resolution partly because biologic motion is absent and because imaging times can be extended for maximum resolution without concern for survival. Thus, for many types of studies, MRM of specimens can improve imaging throughput by eliminating the maintenance and monitoring needed for a live animal.

MRM requires specialized specimen preparation techniques to achieve maximum resolution, tissue/organ contrast, and structural definition. For instance, organs in a formalin-fixed specimen reveal relatively little structural detail, whereas exquisite anatomic detail becomes apparent with the aid of MR contrast agents specifically applied to stain the specimen (Figure 4). An important distinction from conventional histologic methods is that MRM achieves fixation and staining with a single solution that contains both the fixative and a Gd-based contrast agent. The fixative is either Bouin's (LabChem, Pittsburgh, PA) or 10% neutral buffered formalin (Form), and the contrast agent is ProHance (Bracco Diagnostics, Princeton, NJ). We abbreviate these fixative/staining solutions as Bouins-Gd and Form-Gd, and mix each in a ratio of 20:1. The solution is delivered to the various organ systems in the body by several different methods (discussed below), such as immersion (Petiet et al. 2007), bulk injection, and vascular perfusion; the choice of method depends on the particular organ system and stage of development.

Studies of pre- and postnatal development illustrate the power of fixed specimen imaging. This capability, especially in mice, offers a unique opportunity to study normal development as well as teratologic and toxicologic processes. Rat and mouse embryos and fetuses are harvested from the anesthetized dam, cooled, and immersed in a solution of Bouins-Gd. The solution penetrates the entire specimen sufficiently during the early stages of development (up to 18 days gestation) to achieve complete fixation and staining. Images of fixed prenatal embryos are shown in Figure 5A and B, depicting embryonic (E) days E13.5 and E18.5. At the earliest stage (E13.5), relatively little organ differentiation has occurred and it is difficult to identify structures, although mesencephalic vesicle, cardiac, and hepatic structures are apparent. At the later stage (E18.5), familiar structures clearly emerge: the left and right ventricles of the heart, right atrium, liver, and salivary glands, among others. The ability to image the whole body at these early stages of development is particularly important for

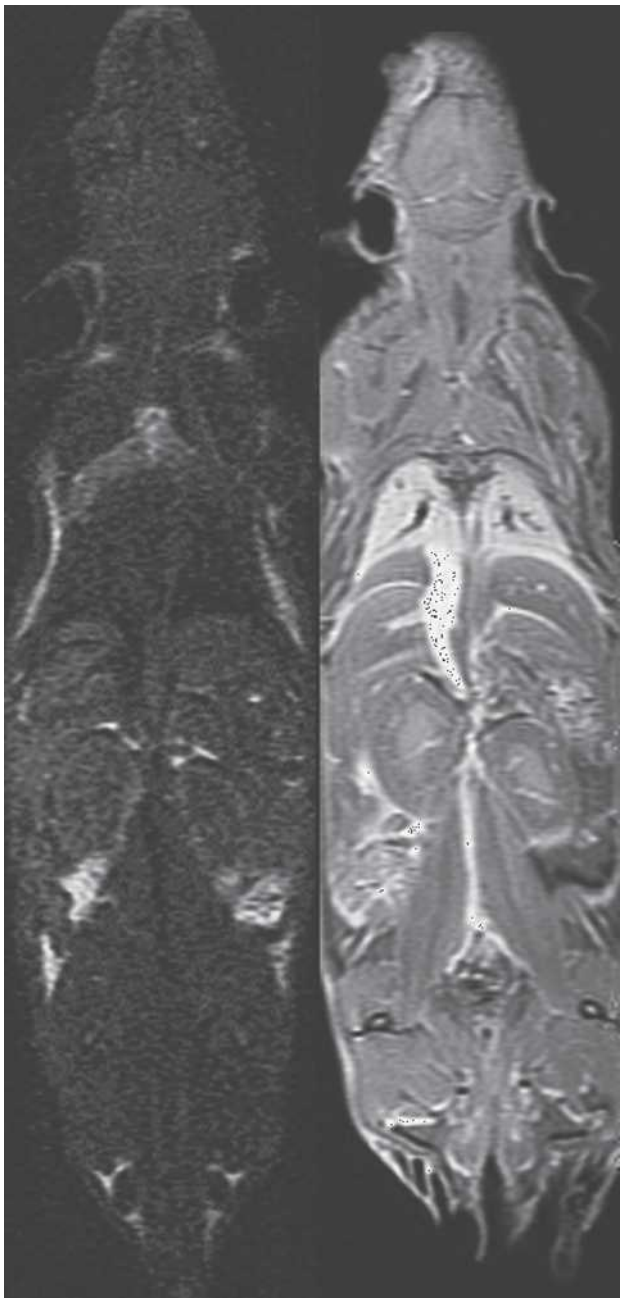

Figure 4 Coronal 2-mm-thick sections were acquired in a formalin-fixed specimen (left) and a specimen stained with a 1:20 mixture of gadopentetate dimeglumine and formalin (right). At TR of 100 ms, the gain in signal-to-noise ratio is fivefold for all tissues except fat. Reprinted with permission from Johnson GA, Cofer GP, Gewalt SL, Hedlund LW. 2002. Morphologic phenotyping with MR microscopy: The visible mouse. Radiology 222:789-793.

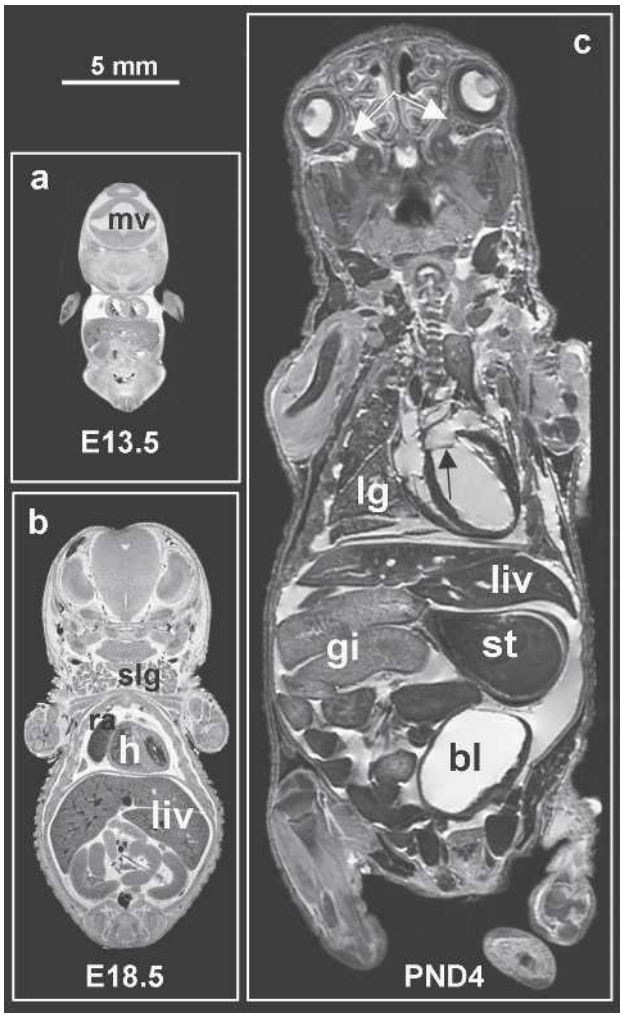

Figure 5 Sample mid-coronal slices of (A) a 13.5-day embryo, (B) an 18.5-day fetus, and (C) a 4-day pup. The two prenatal specimens were prepared by immersion in Bouins fixative with MR contrast ProHance (20:1, v/v), and the postnatal specimen was prepared by ultrasound-guided transcardial perfusion of fixative and stain. All three specimens show the liver (liv), parts of the gastrointestinal tract (gi), and left and right ventricles of the heart (h). Blood appears in the heart of the two prenatal specimens but not in the postnatal one as it was flushed out during perfusion. The E13.5 embryo also shows the mesencephalic vesicle (mv), a precursor of the brain's ventricular system. The E18.5 fetus shows the right atrium (ra) and salivary glands (slg). The PND4 shows part of the right lung (lg), the bladder (bl), and the stomach (st) as well as much smaller structures such as the left/right optic nerves (white arrows) and the mitral valve (black arrow). All three specimens were imaged in a 9.4 T scanner, using a matrix size of 1024 × 512 × 512, TR/TE = 75/5.2 ms. The two prenatal specimens were scanned at an isotropic resolution of $(19.5\ \mu m)^3$ over 6 h 22 min, and the postnatal specimen was scanned at an isotropic resolution of $(39\ \mu m)^3$ over 3 h 11 min.

studies of animals with lethal prenatal mutations (Bamforth et al. 2004; Schneider et al. 2003).

Staining by immersion becomes more difficult in neonates and for fetuses older than 18 days as the integument becomes impermeable to the fixative and staining solutions. For these ages and older, fixation and staining must be done either by injection to the intraperitoneal cavity or under the skin or by vascular perfusion. For neonates, ultrasound is

used to guide the percutaneous insertion of the catheter in the left ventricle as shown in Figure 6 (Zhou et al. 2004). This method avoids damaging the thorax, as occurs during a thoracotomy to access the left ventricle. Perfusion begins with a mixture of 0.9% saline and ProHance (Sal-Gd, 20:1, v/v) and continues with Form-Gd. The perfusate is drained via cuts in the jugular veins, femoral veins of the legs. An exemplary image of a 4-day neonate prepared by this method appears in Figure 5C. This kind of high-resolution MRM of fixed mouse neonates provides 3D anatomical detail of structures that complements information available from traditional histology. In addition to many major organs, small structures also are visible, including the optic nerves and the mitral valve (white and black arrows respectively in Figure 5C).

Fixation and staining methods can also be adapted to prepare adult rats and mice for whole body MRM. The adult animals are perfused and stained via the peripheral blood vessels to avoid invasion of major body cavities, which would disturb the anatomy of internal organs. Perfusion uses Sal-Gd and Form-Gd, and begins with the placement of catheters in the right jugular vein and left carotid artery, and then injection of heparin through the jugular catheter to ensure that blood clotting will not occur during the perfusion. Then a solution of warmed Sal-Gd (36° to 37°C) is infused into the jugular catheter with the aid of a peristaltic pump, while blood is withdrawn from the carotid artery as illustrated in Figure 7. This step clears blood from the heart and lungs following the normal direction of blood flow. Next, the sequential perfusion of Sal-Gd and Form-Gd into the left carotid artery and subsequent draining of the fluid from a cut at the cranial end of the right jugular vein ensure clearance of blood and the fixation and staining of the head. Then, to provide for antegrade flow through the abdominal

Figure 6 Perfusion fixation/staining method for neonatal mice. The primary image shows the postnatal day 4 mouse (2.2 grams), lying in a cradle (lower right inset). Surgical anesthesia is maintained by isoflurane delivered by the nose-cone shroud. Immediately above the mouse's chest is a layer of gel and an ultrasound transducer (40 MHz). On the left are the hoses for saline flush and formalin fixation, which are attached to a 30-gauge catheter inserted in the left ventricle and supplied by a syringe pump. The upper left inset shows the monitor display from the ultrasound system (VisualSonics, Toronto, Canada) showing that the catheter (white arrow) has penetrated the chest wall and the tip is in the left ventricle. The upper right inset shows a closer view of the catheter (black arrows) insertion through the gel, into the left ventricle with the ultrasound probe above.

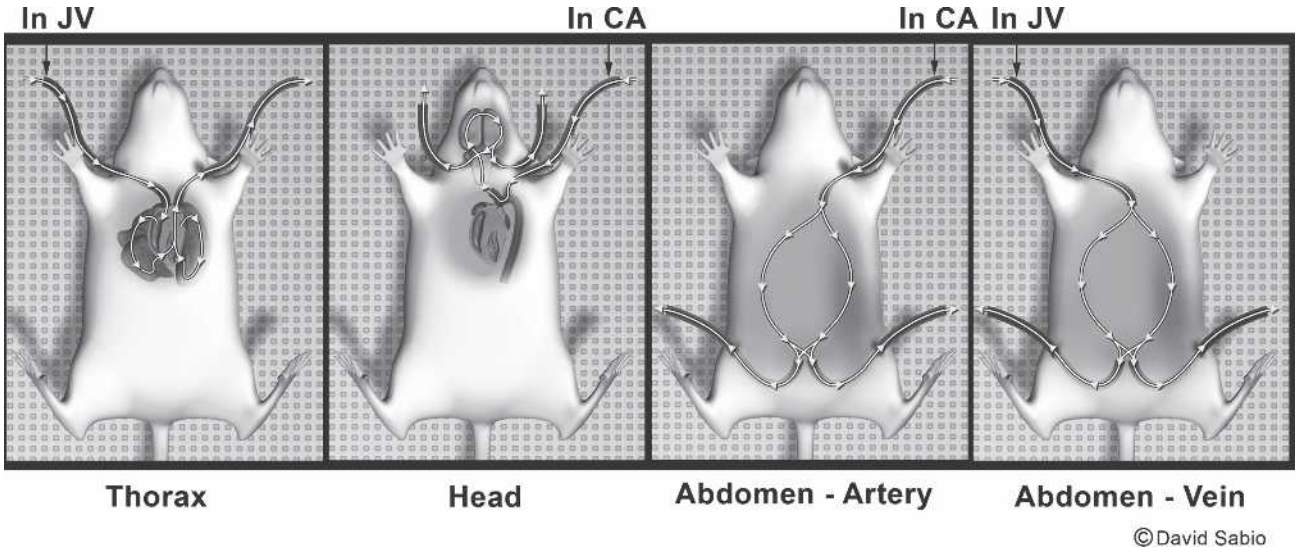

Figure 7 Perfusion fixation/staining method for rats and mice. Catheters are inserted in the right jugular vein and the left carotid artery. The animal is heparinized and then jugular vein infusion begins with saline/Gadolinium (Sal-Gd) while blood is simultaneously withdrawn from the carotid artery to flush the cardiopulmonary system (thorax panel). Second, the head is flushed and fixed by infusion of Sal-Gd followed by formalin/Gadolinium (Form-Gd) into the left carotid artery, with drainage from the cranial jugular veins (head panel). Third, infusion of Form-Gd continues into the carotid artery with drainage from the femoral arteries (abdomen-artery panel). Finally, infusion of Form-Gd continues into the jugular vein (right) with drainage from the femoral vessels (abdomen-vein panel). Figure donated to B. Driehuys by David Sabio, National Institute of Environmental Health Sciences, Research Triangle Park, NC.

arterial system, Form-Gd is pumped into the left carotid artery with primary drainage from the femoral arteries in the legs. Finally, Form-Gd is pumped into the right jugular vein for fixation and staining of the cardiopulmonary and abdominal structures, with primary drainage from the femoral vessels. This stepwise process ensures that all major body organs are fixed and stained without structural damage.

A normal, perfusion-fixed/stained C57BL/6 mouse (19 g) is shown in Figure 8, which depicts four of 2,048 contiguous axial slices through the entire body and illustrates major structures of the thorax and abdomen. This specimen was imaged in a 7-T MR scanner at a 3D isotropic resolution of 63 μm. All of the 2,048 image slices are available in the computer to view slice by slice, which is particularly valuable for following the course of tubular structures such as major systemic blood vessels, pulmonary airways and vessels, and the intestinal tract. Because the image voxels are isotropic, the images can also be viewed in the coronal and sagittal planes. Having the whole body to view in digital form can be valuable in morphologic phenotyping of different genetically altered mouse strains, for detecting metastatic tumors, and in toxicology studies, to name but a few applications (Johnson et al. 2002b; Maronpot et al. 2004).

Animal Preparation, Support, and Monitoring for in Vivo MRM

Without a doubt, the ability to image live animals is one of the most important advantages of MRM. But the natural presence of biologic motion also introduces the most significant obstacle to microscopic resolution. It is essential to control not only gross body movement but also motion that originates from cardiac and breathing activity. With the longer image acquisition times needed to attain high resolution, such motion not only produces image blurring but also can result in artifacts due to spatial encoding errors because the same anatomic structures occupy different positions during the scan. These artifacts often appear as "ghost" artifacts (faint images of the entire structure), which can significantly obscure anatomic detail. For these reasons the animal must be still during imaging and restrained from making gross body movements, such as crawling out of the magnet. Anesthesia ensures this restraint, but anesthetics have the undesirable effect of interfering with body temperature control (Flecknell 1987), and so the animal can quickly lose body heat, especially in the cold bore of the magnet. Exogenous heat is necessary to avoid a drop in the animal's body temperature, and the animal's vital signs must be monitored to maintain normal physiologic status and ensure survival.

Thus animal preparation for MR imaging involves anesthesia, body temperature support, and physiologic monitoring. Depending on the nature of the study, additional support and control may also be necessary, such as respiratory support via mechanical ventilation and gating triggers to synchronize image acquisition with breathing and cardiac motion.

Achieving support, monitoring, and control in MR imaging presents significant obstacles not associated with

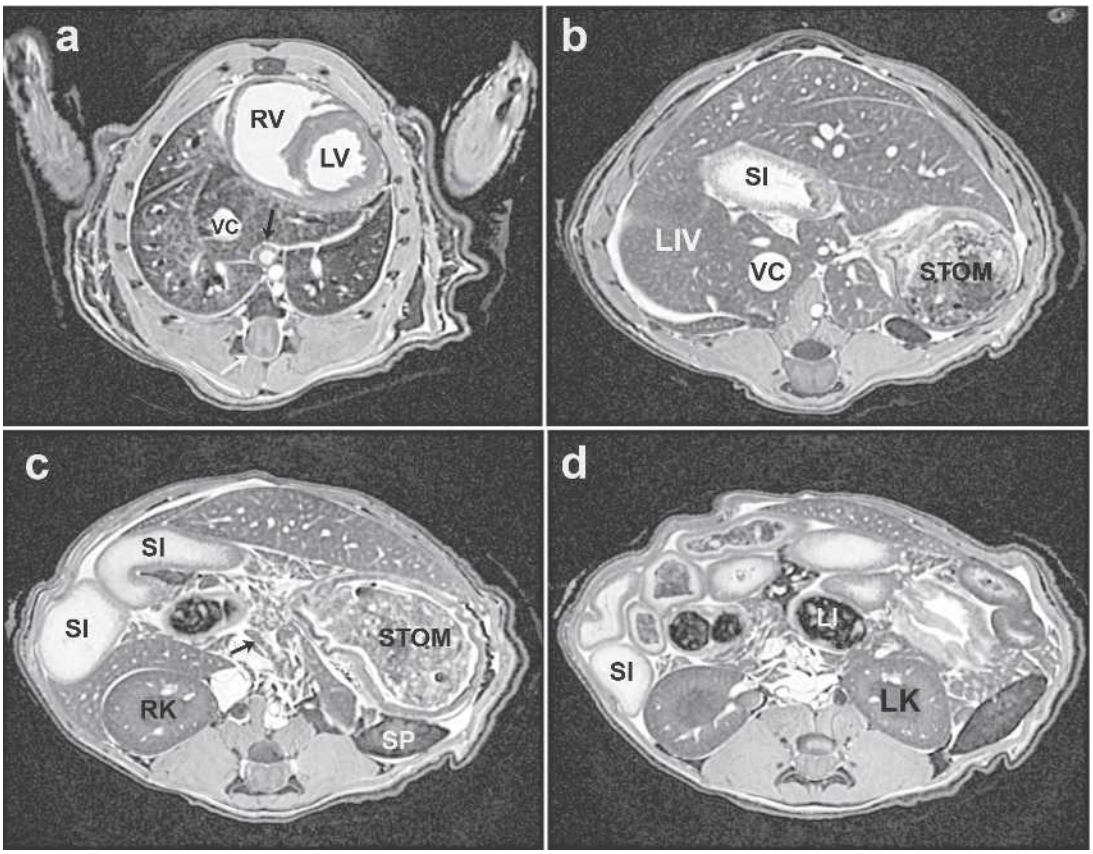

Figure 8 Four representative slices from a perfusion-fixed 19 g C57BL/6 mouse, imaged at 7 T with in-plane resolution of 63 × 63 μm^2. (A) Mid-thoracic level showing the vena cava (VC) in the accessory lobe of the right lung and, below, the main bronchus of the middle lobe of the right lung (dark area). The black arrow points to the circular profiles of the esophagus, abdominal aorta, and azygous vein (in order). Also seen are the right and left ventricles (RV, LV) of the heart. The lower white arrow points to the spinal cord, which is seen in all panels. (B) Upper abdominal level image showing liver lobes surrounding a loop of the small intestine (SI), vena cava (VC), and the stomach (STOM) to the animal's left. (C) Image slice from slightly lower in the abdomen showing more loops of the small intestine (SI) and part of the stomach (STOM), as well as the right kidney (RK), a section of the spleen (SP), and fragments of the pancreas (arrow). (D) Further into the abdomen the right kidney and also the left kidney (LK) are visible, as well as loops of the large intestine (LI), which are dark because of the lack of water, fragments of the pancreas, and a section of the spleen to the animal's left.

other modalities—strong magnetic fields, rapidly switching gradients, and inaccessibility of the animal during imaging. These conditions usually mean that most conventional animal monitoring and support devices cannot be used or must be significantly modified, although in the past few years MR-compatible equipment has become commercially available (SA Inc., Stony Brook, NY; CWE, Ardmore, PA) to make support and monitoring easier to manage.

Anesthetics for chemically restraining animals can be either inhalational or injectable. The former has the major advantage of ease of control, as with isoflurane (Halocarbon Products Corp., River Edge, NJ), which is rapidly taken up by pulmonary circulation and delivered to the central nervous system for effect (Brunson 1997). Because gas exchange occurs quickly, changes to the level of anesthesia can be made quickly and recovery from the anesthesia is rapid once delivery ceases. Inhalational anesthesia can be administered either by nose cone or by mechanical ventilation. Controlling the anesthesia level requires a calibrated vaporizer, which is relatively easy to attach to a nose cone using a flow and pressure regulator. This is a convenient route of delivery since rats and mice are obligate nose breathers.

Delivery of isoflurane by mechanical ventilation is somewhat more complicated, requiring an MR-compatible ventilator (Hedlund and Johnson 2002) and endotracheal intubation either transorally or by tracheostomy (Costa et al. 1986; Thet 1983). The combination of mechanical ventilation and endotracheal intubation is also essential for delivery of hyperpolarized gases for lung imaging (Hedlund and Johnson 2002), as described later. Mechanical ventilation has the further advantage of mitigating the respiratory-depressive effects of anesthesia. If mechanical ventilation is used for longitudinal survival studies, intubation should be

done perorally. Endotracheal intubation tubes (16 or 18 gauge for rats, 20 to 24 gauge for mice) can be fashioned from intracatheters (Quick-Cath, Baxter Healthcare Corp., Deerfield, IL) cut to the proper length.

First, the anesthetized animal is placed supine on a 45° slant board and its mouth held open with the aid of a laryngoscope blade equipped with a fiber-optic light. The endotracheal tube is then inserted between the vocal cords as the animal inhales. To intubate a mouse, a strong fiber-optic lamp is positioned on the ventral surface of the neck to illuminate the oropharynx while the endotracheal tube is inserted into the trachea between the vocal cords.

Injectable anesthetics are an appropriate alternative to inhalational anesthetics but, although easier to administer, they are more difficult to control. Intraperitoneal (i.p.) injection is the most common route for induction of anesthesia and also allows for delivery of maintenance doses. Responses to i.p. injection of anesthesia are inherently slower than pulmonary uptake of gaseous anesthesia because injected agents are diluted before reaching the central nervous system because of serosal membrane absorption and hepatic and renal elimination. Intravenous administration of injectable anesthesia is also possible, for example by a tail-vein injection or indwelling catheter. Popular choices for injectable anesthetics include methohexital for ultrashort procedures (less than 15 minutes), and pentobarbital combined with ketamine/diazepam or ketamine/xylazine for longer procedures. When using ketamine combinations, especially with xylazine, maintenance doses should be given with ketamine alone because of the risk of bradycardia effects from xylazine overdosage. For exact doses, routes, and durations of injectable drugs, we advise the reader to consult available sources (Flecknell 1987; Plumb 2005; Wixson and Smiler 1997).

Regardless of the type of anesthesia used, the combination of the MR imaging environment, cryogenically cooled magnets, depressive effects of anesthesia, and loss of body temperature control requires a supply of exogenous heat. This is especially the case with anesthetized mice, whose large surface area-to-body mass ratio causes body temperature to fall rapidly, so it is essential to provide continual support for body temperature. Effective temperature-control solutions for the table top are heat lamps with temperature feedback controllers (DigiSense, Cole-Parmer Instrument Co., Vernon Hills, IL) or microwavable heat pads (SnuggleSafe, Littlehampton, West Sussex, UK). When animals are placed in the magnet, their body temperature can be monitored by an endorectal thermistor, which provides feedback control for warm air directed through the bore (Qiu et al. 1997).

Effective maintenance of the animal's physiologic status during imaging requires continuous monitoring, at a minimum for body temperature, heart rate, and breathing rate. Custom systems can be made MR-compatible or commercial MR-compatible systems are available for monitoring ECG, breathing, body temperature, and peripheral pulse (SA, Inc., Stony Brook, NY). As long as body temperature is normal and constant, changes in cardiac or breathing rates can serve as indices of anesthesia level: increases in cardiac and/or breathing rates are signs that additional anesthesia is necessary.

At the completion of imaging, the animal's recovery will be hastened by maintaining normal body temperature with heat lamps or heating pads. During this time, continued body temperature monitoring is essential to avoid overheating. Also, to ensure unobstructed breathing, it may be necessary to aspirate any excess fluid in the oral cavity. Because animals may become dehydrated during imaging and unable to drink afterward, the subcutaneous delivery of fluids (e.g., saline, lactated Ringer's) may aid recovery.

A final consideration in animal imaging is the physical support of the animal in a stable, repeatable position. Semicircular cradles are the most effective means to accomplish this because the animal body is nominally cylindrical, as is the RF coil into which it is inserted for the imaging (Figure 3). Cradles can also be fashioned to include built-in nose cones for anesthesia delivery, ECG electrodes for heart monitoring, pneumatic pillows for respiration monitoring, and body temperature probes (Dazai et al. 2004). Such physical support cradles with expanded monitoring capability can also expedite animal setup and improve imaging throughput. In addition, cradles can facilitate multimodality imaging by allowing the animal to be moved from one imaging system to another while maintaining monitoring, physiologic support, and physical position and at the same time ensuring image registration.

Cardiac MRM

The organ that provides perhaps the greatest challenges for in vivo MR microscopy is the rodent heart. The first challenge is simply its size—the rat heart is about the size of the last segment of the human pinky, and that of the mouse spans about the width of a pinky nail. Resolving a structure this small poses a significant SNR challenge, even in the absence of motion. The heart, however, is anything but still, with normal heart rates of 500 to 600 beats per minute for mice (100 milliseconds between beats) and 300 beats per minute for rats (200 milliseconds between beats). Compare these rates to the average adult human heart rate of 60 beats per minute and the challenge becomes apparent.

To image the heart without major artifacts, it is necessary to "freeze" cardiac motion by acquiring image data during precisely timed intervals of the cardiac cycle (Cassidy et al. 2004). Furthermore, because functional information is desired, the heart must be imaged at multiple phases, from systole to diastole. Finally, because image acquisition occurs over the course of many beats, the heart rate must be constant for the duration of the scan. An additional challenge is thoracic movement due to breathing, which occurs in rodents with frequencies ranging from 60 to 120 breaths per minute.

One solution to these problems is to use MR acquisition

sequences that are resistant to motion. For example, radial acquisition captures each line of image data within a fraction of a heartbeat (1 ms), which makes such a sequence resistant to motion by virtue of its very short TE and TR (Brau et al. 2004). A full image is then built up by using cardiac gating to acquire 800 or more image lines (for a 2D image) at the same phase of the cardiac cycle, thus effectively freezing the motion. Placement of a small surface coil on the animal's chest addresses the problem of SNR. This coil is among the simplest coils to build and its small size relative to a whole body coil enhances its sensitivity. However, surface coils sacrifice some image homogeneity, which can be retained more effectively by more sophisticated designs such as the half-birdcage coil (Fan et al. 2006). To image the heart with both high spatial and temporal resolution requires exceptionally strong and rapidly switching gradients. We use peak gradients of 77 Gauss/cm, a nearly fiftyfold increase compared to those on a clinical system.

These techniques make it possible to obtain high-quality images of mouse hearts and to capture the 100 ms beat-to-beat cardiac cycle in as many as forty phases. More typically only ten phases are acquired, which reduces the effective temporal resolution but also shortens the time for image acquisition. This tradeoff increases the available time window to acquire the image lines of each phase and hence to build up the image more quickly.

Initial work in the imaging of cardiac function in the rodent focused on 2D imaging of a single slice through the heart (Brau et al. 2004). 2D images showed excellent contrast between the blood and myocardium because fresh magnetization was continually carried into the image slice by the flowing blood. However, the transition to 3D imaging eliminates such magnetization in-flow because all tissues experience the RF pulses and thus all magnetization is equally depleted. To differentiate the blood from myocardium in 3D imaging one solution is to supply a contrast agent that preferentially enhances blood over myocardium. A particularly useful agent for this is a novel Gadolinium-based nanoparticle contrast agent (Ghaghada et al. 2007). This agent, which remains preferentially in the blood and is not taken up by the myocardium, shortens the blood T_1 while leaving the myocardium T_1 unchanged. After the agent is injected, a T_1-weighted image shows bright blood and dark myocardium, as seen in Figure 9 depicting a 3D image of a C57BL/6 mouse heart. These images were acquired in 15 minutes with a spatial resolution of 87 × 87 × 348 μm^3 and have an effective temporal resolution of 12.4 ms. Such images are readily appreciated in 3D volume renderings, shown in Figure 10.

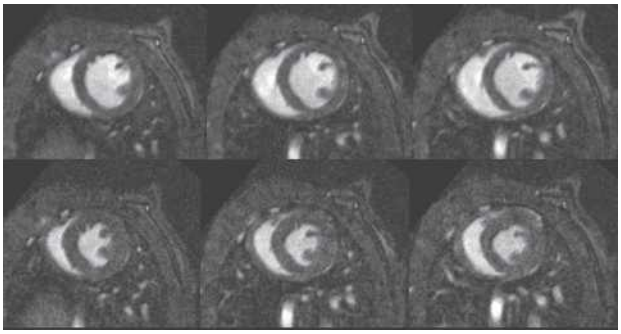

Figure 9 Three short-axis slices of a 3D acquisition of a C57BL/6 mouse heart in diastole (top row) and systole (bottom row). Resolution is 87 × 87 × 348 μm^3 and total acquisition time for the 4D (3D plus time) dataset was 15 minutes. Note the excellent contrast between blood and myocardium that allows for the visualization of papillary muscles and interior structure in the heart.

Figure 10 3D visualization of a C57BL/6 mouse heart at diastole (a) and systole (b). Note the reduced size of the left and right ventricles in systole and the visualization of surrounding blood vessels in the heart.

Improved techniques for rodent cardiac MRM can now be used to extract cardiac performance parameters such as ejection fraction and end-diastolic and end-systolic volumes (Epstein et al. 2002). Cardiac MRM, by virtue of its 3D nature, is beneficial for exact calculations of blood and myocardium volumes (Ruff et al. 1998). MRM is therefore advantageous compared to ultrasound methods that calculate these parameters from 1D measurements of the heart but require assumptions about its 3D shape as well as skilled probe placement, both of which can lead to large error bars. Cardiac MRM, with its associated quantitative power, is particularly useful for phenotyping different mouse strains to show how genetic manipulation can result in valvular defects or septal malformations and associated functional changes (Nahrendorf et al. 2006).

Imaging the Lung

The lungs are typically the last organs to yield quality images with relatively new imaging technologies. Not only are they always moving but the necessary signal source (water protons) is sparse because lungs consist largely of airspaces

(80%) and little tissue (20%). The imaging challenge with MR is further exacerbated by the many air-tissue interfaces in the lung, which reduce the apparent T_2 (known as T_2*) to vanishingly small values (<1 ms). Nonetheless, MR imaging of the lung parenchyma is possible with image acquisition strategies that use ultrashort TE (Gewalt et al. 1993; Shattuck et al. 1997). Beyond lung structure, however, our ultimate interest is in the function of the lung (gas exchange). Recent advances in MR imaging can now reveal the 80% of the lung that we normally do not see! The trick is using breathable gases that provide a strong MR signal.

The ability to visualize gases with MRI is surprising considering that gas is roughly 3,000 times less dense than tissues and should therefore result in a 3,000-fold SNR reduction. Indeed, most gases are ill suited for MRI and yield little or no signal, though some heroic efforts involving fluorinated gases have borne fruit (Kuethe et al. 1998). However, high-resolution gas imaging can be performed using the hyperpolarized (HP[1]) gases ^{3}He and ^{129}Xe. Their MR signals are dramatically enhanced by aligning their nuclear magnetic moments outside the MRI scanner to a level equivalent to what they would attain in a magnetic field of 150,000 T. The method used is called optical pumping and spin exchange, which works by transferring alignment from laser photons to nuclei via an intermediary alkali metal atom (Leawoods et al. 2001). Once the nuclei are aligned, it is possible to preserve the hyperpolarized state for hours or even days (van Beek et al. 2003). The HP gas is then harvested from the device in a delivery bag and administered to the animal by a custom-made ventilator (Chen et al. 2003; Hedlund and Johnson 2002). HP gas MRI can produce images of normal or impaired ventilation in both humans and small animals in exquisite detail. We refer interested readers to a simple overview of ^{3}He and ^{129}Xe hyperpolarization for small animal pulmonary imaging (Driehuys and Hedlund 2007) and excellent clinical reviews (Leawoods et al. 2001; Moller et al. 2002; Salerno et al. 2001).

One of the most natural applications of gas imaging is to use it to visualize the altered distribution of ventilation in cases of pathology, such as asthma or emphysema. In human asthma, HP ^{3}He has been used to visualize subtle and severe deficits in ventilation (Altes et al. 2001) and to show that such ventilation defects can also be elicited by bronchoconstrictive agents such as methacholine (MCh) and subsequently reversed by administration of bronchodilators (Samee et al. 2003). It is also desirable to extend HP ^{3}He MRI to study the fundamental mechanisms of asthma in small animal models. This requires the ability to image and quantify (Spector et al. 2005) the ventilation distribution in small animals with normal breathing and those that are challenged.

Of particular interest is ^{3}He imaging of mice, where transgenic and knockout techniques can be used to create physiologic phenotypes that either mimic human disease or test the involvement of certain pathways and receptors. Recently, we demonstrated 3D imaging of the ^{3}He distribution at 125 × 125 × 1,000 μm^3 resolution in the lungs of a mouse model of asthma before and after challenge with MCh (Driehuys et al. 2007). After MCh challenge, imaging showed constriction of several major bronchi (Figure 11). Such regional information about specific airway involvement in the asthmatic response has never before been available and opens exciting avenues for translational research in this disease area.

Hyperpolarized ^{129}Xe has received less attention than ^{3}He due to the challenges in producing it and its somewhat lower MRI signal. However, in recent years, these technical problems have been addressed to the point that the unique functional information offered by ^{129}Xe (Oros and Shah 2004) can be extracted. Like ^{3}He, ^{129}Xe can be used to make high-quality images of airspaces. However, its most valuable properties are its solubility in tissues and fluids and its ability to be distinguished in different molecular environments by a characteristic shift in its resonant frequency. For example, in the lung, ^{129}Xe exhibits three distinct resonant frequencies: in the airspaces, in the interstitial spaces, and in the red blood cells (RBCs). We recently exploited these frequency shifts to image the transfer of ^{129}Xe gas from alveoli into the blood-gas barrier and to the RBCs (Driehuys et al. 2006). Such differential imaging of these three compartments, shown in Figure 12, appears to be extremely sensitive to pulmonary gas exchange abnormalities. These were created by unilateral instillation of bleomycin, which caused thickening of the blood-gas barrier that impaired the diffusive transfer of ^{129}Xe to the RBCs, leading to an absence of ^{129}Xe signal in the injured left lung (Figure 12F). Such gas exchange imaging could be useful in the study of a large variety of models of chronic obstructive pulmonary disease (COPD), interstitial disease, inflammation, or radiation-induced fibrosis.

Imaging the Brain

Compared to the heart or lung, the brain is an ideal organ for imaging as it involves little gross motion and the head can be physically stabilized. Imaging the rodent brain nondestructively at high resolution is particularly useful in studies of genetically manipulated animals and provides valuable morphologic information about neurological diseases that are often characterized by subtle structural changes. A continuing challenge in brain imaging, however, is to create sufficient contrast, because conventional contrast agents do not penetrate the blood-brain barrier (BBB). Highly specialized techniques and often exogenous contrast agents are necessary to reveal structural detail based on nuclei, fiber tracts, and ventricular spaces.

A typical in vivo rat brain image is shown in Figure 13. This dataset was acquired at 7 T over a span of 40 minutes with a resolution of 250 × 250 × 1,000 μm^3. In vivo brain imaging enables the viewing of several major structures, including the olfactory bulbs (OB), cerebellum (Cblm), corpus callosum (cc), anterior commissure (ac), hippocampus

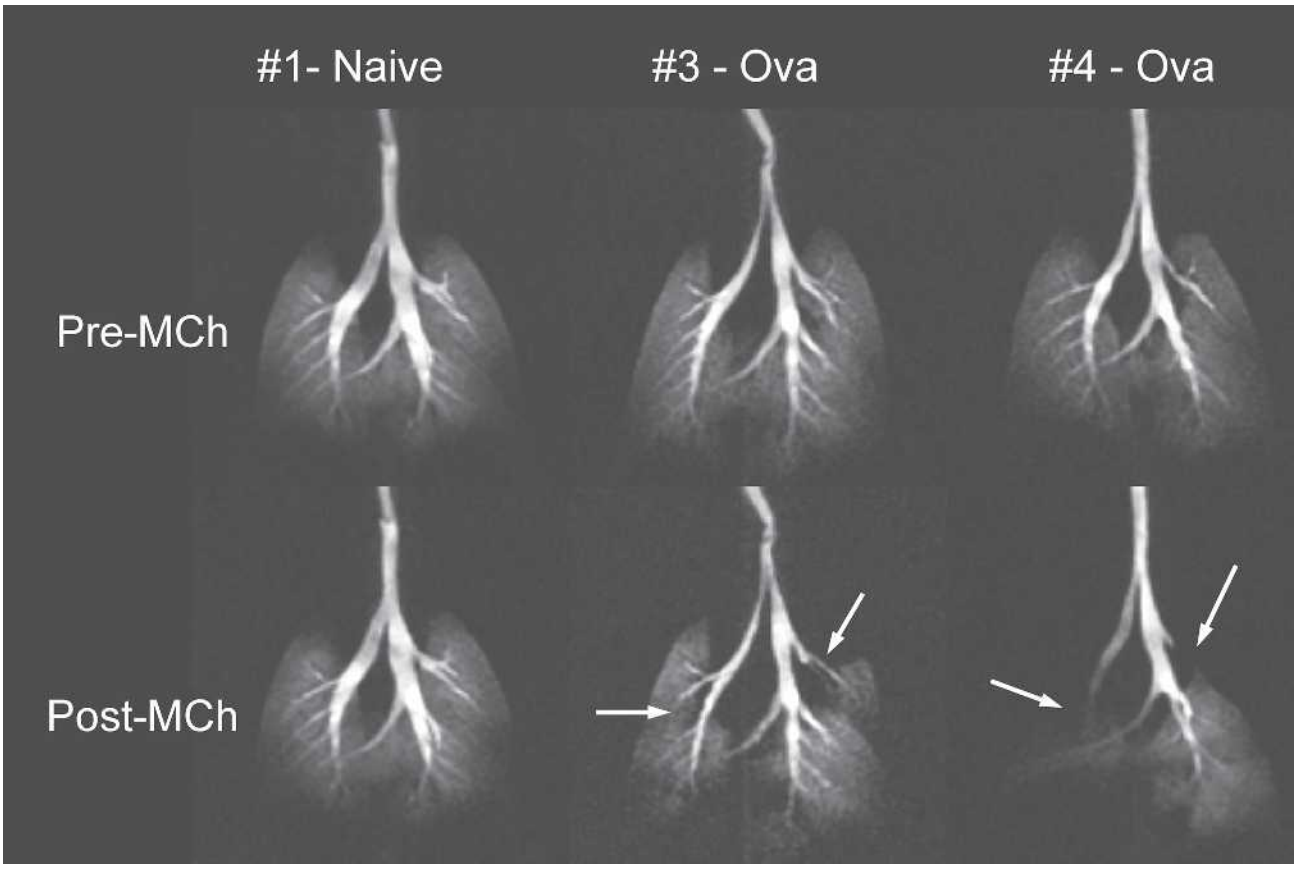

Figure 11 3D ^{3}He images of three BALB/C mice represented as maximum intensity projections. Top row shows mice before and bottom row shows mice after challenge with 250 μg/kg methacholine (MCh) to induce broncho-constriction. From left to right in the figure are one naïve mouse and two mice sensitized to ovalbumin to exhibit asthma. The ova-sensitized mice respond to MCh with severe narrowing of several major airways. Such regional visualization of ventilation redistribution is a powerful new tool in asthma research. Images were acquired using a 3D radial sequence with 125 × 125 × 1000 μm^3 resolution in 5.8 min, FOV = 32 × 32 × 16 mm^3, matrix = 256 × 256 × 16, TR/TE = 5/0.2 ms. Reprinted from Driehuys B, Walker JK, Pollaro J, Cofer GP, Mistry N, Schwartz DA, Johnson GA. 2007. Hyperpolarized 3He MR imaging of methacholine challenge in a mouse model of asthma. Magn Reson Med 58:893–900.

(HC) and its dentate gyrus (DG), medial lemniscus (ml), superior and inferior colliculi (SC, IC), and ventricles (vent). In vivo brain imaging is particularly valuable in longitudinal progression studies that involve disease models (Benveniste and Blackband 2002), the effects of drugs (Lu et al. 2007), and cell migration (Shapiro et al. 2006).

The image resolution and contrast attainable in vivo are sufficient for many biological studies, but numerous investigations demand the high resolution attainable only in fixed brain specimens. For example, many genetically modified animals exhibit abnormalities in certain brain structures that are only 10 to 20 μm in size. To better detect these subtle neuroanatomical variations, the spatial resolution and structural contrast of MRM can be enhanced through variants of the contrast-infused fixation methods previously described. Fixation of brain specimens faces the additional hurdle of requiring the contrast medium to penetrate the blood-brain barrier. This is achieved by first flushing the blood from the head and then perfusing the head with a mixture of warmed Sal-Gd followed by Form-Gd fixative. Although the mechanism by which Gd crosses the BBB remains to be elucidated, its efficacy is evident from the excellent T_1 and T_2 contrast seen in the stained brain image of Figure 14.

Images of the Gd-stained fixed brain, either in the cranium or excised from it, are acquired using a 3D spin echo sequence requiring a scan time of 2 hours to yield an isotropic resolution of $(21\ \mu m)^3$. This type of high-resolution imaging uses numerous technical tricks, including nonuniform radial gain and asymmetric data collection (Johnson et al. 2007). These images can be augmented with T_2-weighted images that accentuate the contrast between different brain structures (Sharief and Johnson 2006). Such multicontrast scans, acquired at $(43\ \mu m)^3$ resolution, were instrumental in driving an automated brain segmentation method (Ali et al. 2005) that identified 33 brain structures (Figure 14). Structures that are now detectable and quantifiable, several of

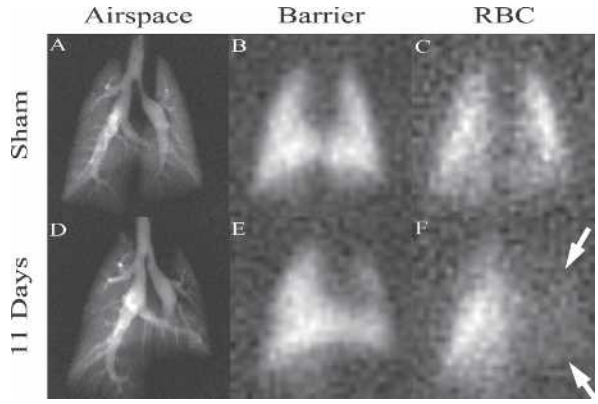

Figure 12 Hyperpolarized ^{129}Xe MR images in three compartments of the lung. The ability to separately image uptake of ^{129}Xe from the pulmonary airspaces (A,D) into the pulmonary tissue barrier (B,E) and red blood cells (C,F) is especially powerful for detection of gas exchange impairment. Such impairment is evident in (F), where ^{129}Xe uptake in red blood cells has been diminished by inflammation and fibrosis caused by instillation of bleomycin. This agent creates thickening of the blood-gas barrier, causing ^{129}Xe (or oxygen) to take longer to reach the red blood cells. Such direct visualization of gas exchange is uniquely enabled by the large frequency shift of ^{129}Xe, which allows separate imaging of the three compartments. Images were acquired using a 2D radial sequence with 0.3 × 0.3 mm^2 resolution in airspaces and 1 × 1 mm^2 in tissues in a time of 2 min. Reprinted from Driehuys B, Cofer GP, Pollaro J, Boslego J, Hedlund LW, Johnson GA. 2006. Imaging alveolar capillary gas transfer using hyperpolarized 129Xe MRI. Proc Natl Acad Sci U S A 103:18278-18283.

which were not included in previous MRM-based brain atlases (Kovacevic et al. 2005; Ma et al. 2005), include the deep mesencephalic reticular nucleus and red nucleus (DpMe); thalamic nuclei, including the ventral posterior and lateral thalamic nuclei (VT); anterior pretectal nucleus (APT); lateral dorsal nucleus (LD); geniculate bodies (Gen); trigeminal tract; pons; cochlear nucleus; substantia nigra; and lateral lemniscus.

An example of high-resolution morphological phenotyping with MRM can be seen in Figure 15, which depicts the reeler mouse (Falconer 1951), a neurodevelopmental model proposed for neurological and psychiatric conditions. Images of brains in reelin (*Reln*)-deficient mice and wild-type (WT) control mice were acquired using a T_1-weighted MRM protocol. A marked difference was observed in *Reln*$^{rl/rl}$ mice, which exhibited a smaller brain compared to WT controls. Furthermore, both *Reln*$^{rl/+}$ and *Reln*$^{rl/rl}$ mice exhibited larger ventricles compared to WT controls. *Reln*$^{rl/rl}$ and WT brain structures also showed shape differences in the cerebellum, olfactory bulbs, dorsomedial frontal and parietal cortex, certain regions of temporal and occipital lobes, the lateral ventricles, and the ventral hippocampus. These findings suggest that the *Reln* mutation may affect certain brain regions more severely than others, and this example shows that high-resolution anatomical phenotyping by MRM is clearly poised to play a significant role in understanding how specific gene mutations affect brain organization (Badea et al. 2007).

Although we have covered only high-resolution anatomical brain imaging, numerous other powerful types of contrast mechanisms are available. For example, diffusion tensor imaging (DTI) (Mori and Zhang 2006) uses the fact that water diffusion is spatially constrained to map the fiber tract architecture of the brain. DTI is enormously powerful for the study of CNS disorders involving white matter tracts and demyelination (Chahboune et al. 2007). Another powerful tool long recognized in clinical MRI is functional MRI (fMRI), which is now reaching the stage of application to animal models. fMRI has been applied with success to the study of the visual (Huang et al. 1996) and somatosensory systems (Ahrens and Dubowitz 2001) of the mouse.

Current and Future Research Directions

MRM continues to present opportunities to enhance image SNR and contrast, and to improve resolution and specificity. While the small samples imaged in MRM contribute less signal compared to clinical subjects, they also tend to contribute little or no noise except at very high frequencies. Instead, the RF coil is often the primary contributor of image noise in MRM (Black 1993). Coil noise is proportional to both the coil resistance and its absolute temperature and therefore can be dramatically reduced with the use of superconducting or cold copper RF coils. Unlike conventional copper coils, superconducting coils present negligible resistance and a very low absolute temperature, thereby drastically reducing the amount of noise that contaminates the image. Their low resistance endows them with a very high quality factor (Q) and results in larger signals and a higher SNR.

Though conceptually appealing, the practical implementation of superconducting coils has taken more than a decade of dedicated effort because specialized superconducting coil design techniques are necessary in order to make production costs and turnaround times practical. Furthermore, cryogenic temperature regulation must be very stable to avoid frequency shifts and abrupt changes in Q (Hurlston et al. 1999; Miller et al. 1999), both of which can cause image artifacts. It is also important to make the coil's radiofrequency field sufficiently homogeneous by choosing appropriate dielectric materials and understanding second-order electromagnetic effects in superconducting coils. These coils may transfer radiofrequency power nonlinearly during pulse transmission, making slice selection and variable flip angles difficult to implement. Radiofrequency simulations may provide valuable guidance during the design process (Nouls et al. 2006).

When the technical challenges have been successfully addressed, reports describe SNR improvements ranging from a factor of 3 (Hurlston et al. 1999; Nouls et al. 2006) to as much as 10 (Black et al. 1993). Such improvements

Figure 13 In vivo imaging of the rat brain at a resolution of 250 × 250 × 1000 μm^3. The top row shows horizontal slices progressing from dorsal to ventral. The bottom row shows axial slices progressing in the rostral to caudal direction. The images reveal several structures including the olfactory bulbs (OB), cerebellum (Cblm), caudate putamen (CPu), substantia nigra (SN), corpus callosum (cc), anterior commissure (ac), interpeduncular nucleus (IP), hippocampus (HC) and its dentate gyrus (DG), medial lemniscus (ml), superior and inferior colliculi (SC, IC), and ventricles (vent). All images were acquired using a 3D spin echo protocol at 62.5 kHz bandwidth and a matrix of 256 × 128 × 32. The top row images were acquired with FOV = 64 × 32 × 32 mm^3, TR/TE = 1500/4.0 ms. The bottom row images were acquired with FOV = 40 × 40 × 45 mm^3, TR/TE = 400/5.1 ms.

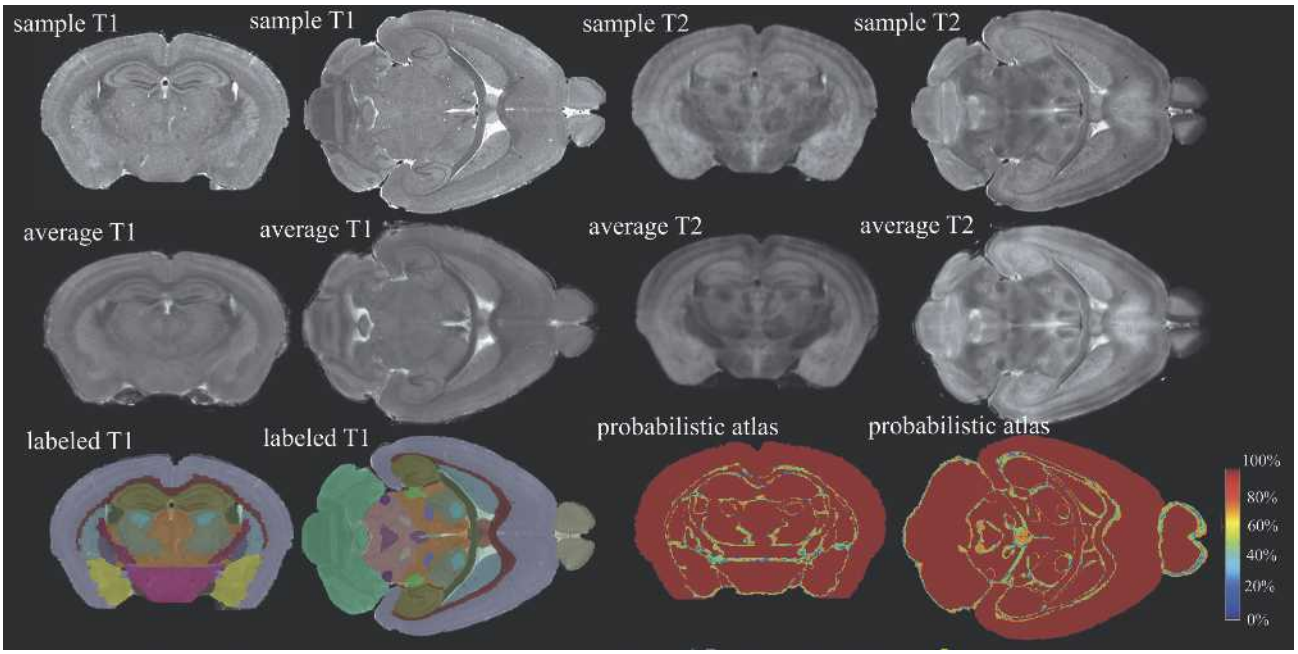

Figure 14 MRM is used to create a labeled atlas for the C57BL/6 mouse brain. The top row shows axial and horizontal image slices of T_1- and T_2-weighted datasets from fixed brain specimens acquired with $(21.5\text{-}\mu m)^3$ resolution. Such images from multiple brains are co-registered and combined to create average brain images (middle row), which are then segmented to identify individual brain structures and create a labeled atlas (bottom row, 1st and 2nd columns). An additional measurement of interest is the variability of structures within the species. Variability is captured in a probabilistic atlas (bottom row, 3rd and 4th columns), which exhibits in each voxel the level of agreement of all labels in all brains. Regions of low agreement are found at the border of structures and in regions where small structures are in close vicinity. All images were acquired with a 3D spin echo sequence, matrix size of 1024 × 512 × 512, TR/TE = 50/5.2 ms.

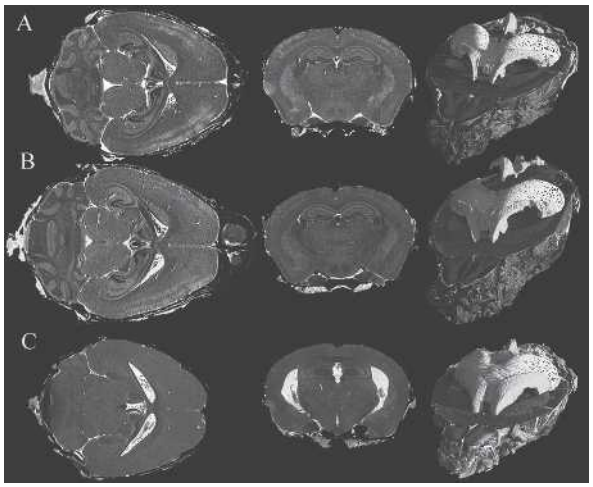

Figure 15 T_1-weighted images of the brains of (A) wild-type (WT) mice and (B) mice with heterozygous and (C) homozygous *Reln* mutation. These images of fixed perfused mouse brains were acquired at $(21.5\ \mu m)^3$ resolution and segmented to show the ventricles and hippocampus. Horizontal sections in the homozygous reeler mutant show severe atrophy in the cerebellum compared to the heterozygous mutant and WT. The heterozygous mutant also shows disturbances in the layered structures of the cortex and hippocampus, as well as enlarged ventricles. The right column shows segmentation of the hippocampus (light gray) and ventricles (dark gray), which indicates shape differences among the three genotypes. Images were acquired using a 3D spin echo sequence with TR/TE = 50/51 ms, FOV = $22 \times 11 \times 11$ mm^3, a $1024 \times 512 \times 512$ matrix.

can reduce image acquisition time, increase sensitivity, or improve spatial resolution, as shown in Figure 16. This figure shows a coronal view of a mouse brain, an image acquired using a superconducting Helmholtz coil pair in 17 hours and with an in-plane resolution of 10 microns. Such

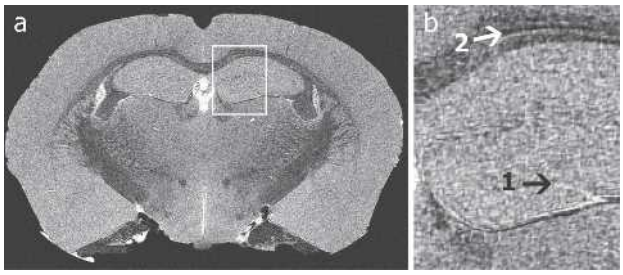

Figure 16 (A) A 10-micron in-plane resolution, coronal slice through the mouse hippocampus. (B) Anatomical features unseen at the resolution achievable with copper coils become apparent: the transitions between layers (arrow 1) in the hippocampus and the layering of the corpus callosum (arrow 2) are visible. Images were acquired using a gradient recalled echo (GRE) sequence, 90° flip angle, TR/TE = 100/5.5 ms, FOV = $21.3 \times 10.6 \times 10.6$ mm^3, bandwidth = 62.5 kHz, resolution of $10 \times 10 \times 20\ \mu m^3$.

resolution would not be possible within reasonable time constraints with the use of a room-temperature copper coil.

In addition to improving spatial and temporal resolution, recent efforts in MRI have been geared toward probing beyond anatomy and function down to the molecular level. This "molecular imaging" (Weissleder and Mahmood 2001) is an area of active research in all imaging modalities and is defined as "visualization, characterization, and measurement of biological processes at the molecular and cellular levels." Although molecular imaging has predominantly used more sensitive nuclear imaging methods, such as positron emission tomography (PET) and single photon emission computed tomography (SPECT), there are certain advantages to MRI (Sosnovik and Weissleder 2007). For example, MRI can add exquisite anatomical and functional information to provide context for the usually fuzzy molecular picture. Furthermore, in MRI the contrast can be "turned on" in response to a specific event (Lowe 2004), whereas it is not possible to similarly manipulate signal from the nuclear methods.

The primary focus of molecular imaging with MRM is to develop contrast agents (probes) that can report on molecular events or targets of interest. However, these targets are often present at only very low concentrations, so their detection requires the development of probes whose presence can be amplified when they have reached their objective (Querol and Bogdanov 2006). Probes for molecular imaging contain either a paramagnetic (Gadolinium) or superparamagnetic (iron) moiety that acts as a T_1, T_2, or T_2* contrast agent, but they also include specific molecular structures that cause the probes to target and accumulate in areas where specific molecular or cellular processes are most prolific. For example, targeted probes have been reported for imaging atherosclerotic plaques via surface integrins (Winter et al. 2003), tumor vasculature via surface receptors (Sipkins et al. 1998), and cell apoptosis (Zhao et al. 2001). Probes that activate in response to an event include those for sensing pH (Lowe et al. 2001) or enzymatic activity (Louie et al. 2000). Another important aspect of molecular imaging to which MRM is particularly well suited is the tracking of cells to study cell and gene therapy (Bulte and Kraitchman 2004; Ho and Hitchens 2004).

As a final note, we would be remiss if we did not point out that image acquisition is only the first step in applying MRM to biological problems. After collection of the image data, a further challenge is to extract the most relevant and sensitive measures of interest. This can be a daunting challenge when data consist of $512 \times 512 \times 512$ pixels each containing 16 bits of grayscale information. Image analysis is vitally important, and is in fact the subject of active research. Effective image analysis can include co-registration of serial images or those from multiple modalities, image segmentation to identify key structures, image enhancement to accentuate desired features, and, most importantly, image quantification to enable researchers to distill these complex datasets into numbers that can be used to study the problem at hand. We refer the interested reader to

Gonzalez and Woods (2006) as a starting point for more information about this important topic.

Conclusion

Magnetic resonance microscopy has become a stable and ubiquitous platform for biomedical investigations and occupies a unique position in the pantheon of small animal imaging modalities. The choice of imaging modality is a complex one that requires consideration of all aspects of a project, and with so many imaging modalities now available, researchers have to determine when and whether to use MRM rather than microCT, for example. MicroCT enjoys the advantages of generally higher throughput, lower cost, and exquisite resolution—as low as 6 to 8 μm for fixed specimens (Johnson et al. 2006) and 100 μm for in vivo imaging (Badea et al. 2004). However, CT requires a high x-ray dose, which constrains its use in longitudinal studies. A further limitation is that the contrast available for CT is limited primarily to differences in tissue density and therefore molecular imaging with CT has not yet made much headway.

MRM, on the other hand, benefits from its noninvasive, 3D capacity and its high resolution for both anatomic and functional images. Perhaps its greatest asset is its extraordinary richness of contrast, which is now being pushed toward the molecular imaging level. The challenges of MRM continue to be the expense of the equipment, the specialized MR physics knowledge required to get the most out of a scanner, the time required to acquire an image, and therefore low throughput. It is likely, however, that many of these challenges can be overcome with technical development efforts taking place in laboratories around the world and that MRM may become the modality of choice for many biomedical investigations. Particularly exciting developments include the increase in throughput enabled by the capacity to image multiple mice simultaneously (Bock et al. 2003; Nieman et al. 2005), as well as possibilities offered by technologies such as superconducting coils, hyperpolarized gases, and molecular imaging probes.

There are thus ample opportunities to keep both MRM technology developers and biomedical investigators productively engaged.

Acknowledgments

The authors thank Sally Zimney for assistance in the preparation of the manuscript and Al Johnson for fostering many of the developments reviewed in this article. This work was performed at the Duke Center for In Vivo Microscopy, an NCRR/NCI National Biomedical Technology Resource Center (P41 RR005959/U24 CA092656), with additional support from NIH/NHLBI (R01 HL055348), NIH/NIBIB (1 T32 EB001040), the Mouse Bioinformatics Research Network (MBIRN)—NIH/NCRR (U24 RR021760), and the GEMI Fund 2005.

References

Ahrens ET, Dubowitz DJ. 2001. Peripheral somatosensory fMRI in mouse at 11.7 T. NMR Biomed 14:318-324.

Ali AA, Dale AM, Badea A, Johnson GA. 2005. Automated segmentation of neuroanatomical structures in multispectral MR microscopy of the mouse brain. Neuroimage 27:425-435.

Altes TA, Powers PL, Knight-Scott J, Rakes G, Platts-Mills TAE, DeLange EE, Alford BA, Mugler JP, Brookeman JR. 2001. Hyperpolarized 3He MR lung ventilation imaging in asthmatics: Preliminary findings. J. Magn Res Imag 13:378-384.

Badea C, Hedlund LW, Johnson GA. 2004. Micro-CT with respiratory and cardiac gating. Med Phys 31:3324-3329.

Badea A, Nicholls PJ, Johnson GA, Wetsel WC. 2007. Neuroanatomical phenotypes in the Reeler mouse. Neuroimage 34:1363-1374.

Bamforth SD, Braganca J, Farthing CR, Schneider JE, Broadbent C, Michell AC, Clarke K, Neubauer S, Norris D, Brown NA, Anderson RH, Bhattacharya S. 2004. Cited2 controls left-right patterning and heart development through a Nodal-Pitx2c pathway. Nat Genet 36: 1189-1196.

Beck BL, Blackband SJ. 2001. Phased array imaging on a 4.7T/33cm animal research system. Rev Sci Instrum 72:4292-4294.

Benveniste H, Blackband S. 2002. MR microscopy and high resolution small animal MRI: Applications in neuroscience research. Prog Neurobiol 67:393-420.

Beuf O, Jaillon F, Saint-Jalmes H. 2006. Small-animal MRI: Signal-to-noise ratio comparison at 7 and 1.5 T with multiple-animal acquisition strategies. Magn Reson Mater Phy 19:202-208.

Black RD, Early TA, Roemer PB, Mueller OM, Morgo-Campero A, Turner LG, Johnson GA. 1993. A high temperature superconducting receiver for NMR microscopy. Science 259:793-795.

Bock NA, Konyer NB, Henkelman RM. 2003. Multiple-mouse MRI. Magn Reson Med 49:158-167.

Brau ACS, Hedlund LW, Johnson GA. 2004. Cine magnetic resonance microscopy of the rat heart using cardiorespiratory-synchronous projection reconstruction. J Magn Reson Imaging 20:31-38.

Brunson DR. 1997. Pharmacology of inhalational anesthetics. In: Kohn DF, ed. Anesthesia and Analgesia in Laboratory Animals, Chapter 2. San Diego: Academic Press.

Bulte JWM, Kraitchman DL. 2004. Iron oxide MR contrast agents for molecular and cellular imaging. NMR Biomed 17:484-499.

Bushberg JT, Seibert JA, Leidholdt EM, Boone JM. 2001. The Essential Physics of Medical Imaging, 2nd ed. Baltimore: Williams and Wilkins.

Caravan P, Ellison JJ, McMurry TJ, Lauffer RB. 1999. Gadolinium(III) chelates as MRI contrast agents: Structure, dynamics, and applications. Chem Rev 99:2293-2352.

Cassidy PJ, Schneider JE, Grieve SM, Lygate C, Neubauer S, Clarke K. 2004. Assessment of motion gating strategies for mouse magnetic resonance at high magnetic fields. J Magn Reson Imaging 19:229-237.

Chahboune H, Ment LR, Stewart WB, Ma XX, Rothman DL, Hyder F. 2007. Neurodevelopment of C57B/L6 mouse brain assessed by in vivo diffusion tensor imaging. NMR Biomed 20:375-382.

Chen BT, Brau AC, Johnson GA. 2003. Measurement of regional lung function in rats using hyperpolarized ^{3}helium dynamic MRI. Magn Reson Med 49:78-88.

Costa DL, Lehmann JR, Harold WM, Drew RT. 1986. Transoral tracheal intubation of rodents using a fiberoptic laryngoscope. Lab Animal Sci 36:256-261.

Darrasse L, Ginefri JC. 2003. Perspectives with cryogenic RF probes in biomedical MRI. Biochimie 85:915-937.

Dazai J, Bock NA, Nieman BJ, Davidson LM, Henkelman RM, Chen XJ. 2004. Multiple mouse biological loading and monitoring system for MRI. Magn Reson Med 52:709-715.

Doty FD, Entzminger G, Kulkarni J, Pamarthy K, Staab JP. 2007. Radio frequency coil technology for small-animal MRI. NMR Biomed 20: 304-325.

Driehuys B, Cofer GP, Pollaro J, Boslego J, Hedlund LW, Johnson GA. 2006. Imaging alveolar capillary gas transfer using hyperpolarized 129Xe MRI. Proc Natl Acad Sci U S A 103:18278-18283.

Driehuys B, Hedlund LW. 2007. Imaging techniques for small animal models of pulmonary disease: MR microscopy. Toxicol Pathol 35:49-58.

Driehuys B, Walker JK, Pollaro J, Cofer GP, Mistry N, Schwartz DA, Johnson GA. 2007. Hyperpolarized 3He MR imaging of methacholine challenge in a mouse model of asthma. Magn Reson Med 58:893-900.

Edelstein WA, Glover GH, Hardy CJ, Redington RW. 1986. The intrinsic signal-to-noise ratio in NMR imaging. Magn Reson Med 3:604-618.

Epstein FH, Yang ZQ, Gilson WD, Berr SS, Kramer CM, French BA. 2002. MR tagging early after myocardial infarction in mice demonstrates contractile dysfunction in adjacent and remote regions. Magn Reson Med 48:399-403.

Falconer DS. 1951. 2 new mutants, trembler and reeler, with neurological actions in the house mouse (*Mus musculus* L). J Genet 50:192-201.

Fan XB, Markiewicz EJ, Zamora M, Karczmar GS, Roman BB. 2006. Comparison and evaluation of mouse cardiac MRI acquired with open birdcage, single loop surface and volume birdcage coils. Phys Med Biol 51:N451-N459.

Flecknell PA. 1987. Laboratory Animal Anesthesia: An Introduction for Research Workers and Technicans. San Diego: Academic Press.

Gareis D, Wichmann T, Lanz T, MeIkus G, Horn M, Jakob PM. 2007. Mouse MRI using phased-array coils. NMR Biomed 20:326-334.

Gewalt SL, Glover GH, MacFall JR, Hedlund LW, Johnson GA. 1993. MR microscopy of the rat lung using projection reconstruction. Magn Reson Med 29:99-106.

Ghaghada KB, Bockhorst KHJ, Mukundan S, Annapragada AV, Narayana PA. 2007. High-resolution vascular imaging of the rat spine using liposomal blood pool MR agent. Am J Neurorad 28:48-53.

Gonzalez RC, Woods RE. 2006. Digital Image Processing, 3rd ed. Upper Saddle River NJ: Prentice-Hall.

Haacke EM, Brown RW, Thompson MR, Venkatesan R. 1999. Magnetic Resonance Imaging Physical Principles and Sequence Design. New York: Wiley-Liss.

Hayes CE, Edelstein WA, Schenck JF, Mueller OM, Eash M. 1985. An efficient, highly homogeneous radiofrequency coil for whole body NMR imaging at 1.5 T. J Magn Reson 63:622-628.

Hedlund LW, Johnson GA. 2002. Mechanical ventilation for imaging the small animal lung. ILAR J 43:159-174.

Ho C, Hitchens TK. 2004. A noninvasive approach to detecting organ rejection by MRI: Monitoring the accumulation of immune cells at the transplanted organ. Curr Pharmaceut Biotechnol 5:551-566.

Hornak JP. 2006. The Basics of MRI. Available online at http://www.cis.rit.edu/htbooks/mri/.

Huang W, Palyka I, Li HF, Eisenstein EM, Volkow ND, Springer CS. 1996. Magnetic resonance imaging (MRI) detection of the murine brain response to light: Temporal differentiation and negative functional MRI changes. Proc Natl Acad Sci U S A 93:6037-6042.

Hurlston SE, Brey WW, Suddarth SA, Johnson GA. 1999. A high-temperature superconducting Helmholtz probe for microscopy at 9.4 T. Magn Reson Med 41:1032-1038.

Johnson GA, Cofer GP, Fubara B, Gewalt SL, Hedlund LW, Maronpot RR. 2002a. Magnetic resonance histology for morphologic phenotyping. J Magn Reson Imaging 16:423-429.

Johnson GA, Cofer GP, Gewalt SL, Hedlund LW. 2002b. Morphologic phenotyping with MR microscopy: The visible mouse. Radiology 222: 789-793.

Johnson GA, Ali-Sharief A, Badea A, Brandenburg J, Cofer GP, Fubara B, Gewalt SL, Hedlund LW, Upchurch L. 2007. High-throughput morphologic phenotyping of the mouse brain with magnetic resonance histology. Neuroimage 37:82-89.

Johnson JT, Hansen MS, Wu I, Healy LJ, Johnson CR, Jones GM, Capecchi MR, Keller C. 2006. Virtual histology of transgenic mouse embryos for high-throughput phenotyping. PLoS Genetics 2:471-477.

Kovacevic N, Henderson JT, Chan E, Lifshitz N, Bishop J, Evans AC, Henkelman RM, Chen XJ. 2005. A three-dimensional MRI atlas of the mouse brain with estimates of the average and variability. Cereb Cortex 15:639-645.

Kuethe DO, Caprihan A, Fukushima E, Waggoner RA. 1998. Imaging lungs using inert fluorinated gases. Magn Reson Med 39:85-88.

Leawoods JC, Yablonskiy DA, Saam B, Gierada DS, Conradi MS. 2001. Hyperpolarized He-3 gas production and MR imaging of the lung. Conc Magn Reson 13:277-293.

Louie AY, Huber MM, Ahrens ET, Rothbacher U, Moats R, Jacobs RE, Fraser SE, Meade TJ. 2000. In vivo visualization of gene expression using magnetic resonance imaging. Nat Biotechnol 18:321-325.

Lowe MP. 2004. Activated MR contrast agents. Curr Pharmaceut Biotechnol 5:519-528.

Lowe MP, Parker D, Reany O, Aime S, Botta M, Castellano G, Gianolio E, Pagliarin R. 2001. pH-dependent modulation of relaxivity and luminescence in macrocyclic gadolinium and europium complexes based on reversible intramolecular sulfonamide ligation. J Am Chem Soc 123:7601-7609.

Lu HB, Xi ZX, Gitajn L, Rea W, Yang YH, Stein EA. 2007. Cocaine-induced brain activation detected by dynamic manganese-enhanced magnetic resonance imaging (MEMRI). Proc Natl Acad Sci U S A 104:2489-2494.

Ma Y, Hof PR, Grant SC, Blackband SJ, Bennett R, Slatest L, McGuigan MD, Benveniste H. 2005. A three-dimensional digital atlas database of the adult C57BL/6J mouse brain by magnetic resonance microscopy. Neuroscience 135:1203-1215.

Maronpot RR, Sills RC, Johnson GA. 2004. Applications of magnetic resonance microscopy. Toxicol Pathol 32:42-48.

Miller JR, Hurlston SE, Ma QY, Face DW, Kountz DJ, MacFall JR, Hedlund LW, Johnson GA. 1999. Performance of a high-temperature superconducting probe for in vivo microscopy at 2.0 T. Magn Reson Med 41:72-79.

Moller HE, Chen XJ, Saam B, Hagspiel KD, Johnson GA, Altes TA, de Lange EE, Kauczor HU. 2002. MRI of the lungs using hyperpolarized noble gases. Magn Reson Med 47:1029-1051.

Mori S, Zhang JY. 2006. Principles of diffusion tensor imaging and its applications to basic neuroscience research. Neuron 51:527-539.

Nahrendorf M, Streif JU, Hiller KH, Hu K, Nordbeck P, Ritter O, Sosnovik D, Bauer L, Neubauer S, Jakob PM, Ertl G, Spindler M, Bauer WR. 2006. Multimodal functional cardiac MRI in creatine kinase-deficient mice reveals subtle abnormalities in myocardial perfusion and mechanics. Am J Physiol-Heart C 290:H2516-H2521.

Nieman BJ, Bock NA, Bishop J, Sled JG, Chen XJ, Henkelman RM. 2005. Fast spin-echo for multiple mouse magnetic resonance phenotyping. Magn Reson Med 54:532-537.

Nouls J, Izenson M, Bagley M, Greeley H, Rozzi J, Johnson GA. 2006. A superconducting volume coil for MR microscopy at 9.4 T. 14th Annual Meeting, ISMRM:221.

Oros A, Shah NJ. 2004. Hyperpolarized xenon in NMR and MRI. Phys Med Biol 49:R105-R153.

Petiet A, Hedlund L, Johnson GA. 2007. Staining methods for magnetic resonance microscopy of the rat fetus. J Magn Reson Imaging 25:1192-1198.

Plumb DC. 2005. Plumb's Veterinary Drug Handbook, 5th ed. Ames: Blackwell Publishing.

Qiu HH, Cofer GP, Hedlund LW, Johnson GA. 1997. Automated feedback control of body temperature for small animal studies with MR microscopy. IEEE Trans Biomed Eng 44:1107-1113.

Querol M, Bogdanov A. 2006. Amplification strategies in MR imaging: Activation and accumulation of sensing contrast agents (SCAs). J Magn Reson Imaging 24:971-982.

Ruff J, Wiesmann F, Hiller KH, Voll S, von Kienlin M, Bauer WR, Rommel E, Neubauer S, Haase A. 1998. Magnetic resonance microimaging for noninvasive quantification of myocardial function and mass in the mouse. Magn Reson Med 40:43-48.

Salerno M, Altes TA, Mugler JP, Nakatsu M, Hatabu H, DeLange EE. 2001. Hyperpolarized noble gas MR imaging of the lung: Potential clinical applications. Eur J Radiology 40:33-44.

Samee S, Altes T, Powers P, de Lange EE, Knight-Scott J, Rakes G, Mugler JP, Ciambotti JM, Alford BA, Brookeman JR, Platts-Mills TAE. 2003. Imaging the lungs in asthmatic patients by using hyperpolarized helium-3 magnetic resonance: Assessment of response to methacholine and exercise challenge. J Allergy Clin Immunol 111: 1205-1211.

Schneider JE, Bamforth SD, Farthing CR, Clarke K, Neubauer S, Bhattacharya S. 2003. Rapid identification and 3D reconstruction of complex cardiac malformations in transgenic mouse embryos using fast gradient echo sequence magnetic resonance imaging. J Mol Cell Cardiol 35:217-222.

Shapiro EM, Gonzalez-Perez O, Garcia-Verdugo JM, Alvarez-Buylla A, Koretsky AP. 2006. Magnetic resonance imaging of the migration of neuronal precursors generated in the adult rodent brain. Neuroimage 32:1150-1157.

Sharief AA, Johnson GA. 2006. Enhanced T-2 contrast for MR histology of the mouse brain. Magn Reson Med 56:717-725.

Shattuck MD, Gewalt SL, Glover GH, Hedlund LW, Johnson GA. 1997. MR microimaging of the lung using volume projection encoding. Magn Reson Med 38:938-942.

Sipkins DA, Cheresh DA, Kazemi MR, Nevin LM, Bednarski MD, Li KCP. 1998. Detection of tumor angiogenesis in vivo by alpha(v)-beta(3)-targeted magnetic resonance imaging. Nat Med 4:623-626.

Sosnovik DE, Weissleder R. 2007. Emerging concepts in molecular MRI. Curr Opin Biotechnol 18:4-10.

Spector ZZ, Emami K, Fischer MC, Zhu J, Ishii M, Vahdat V, Yu J, Kadlecek S, Driehuys B, Lipson DA, Gefter W, Shrager J, Rizi RR. 2005. Quantitative assessment of emphysema using hyperpolarized He-3 magnetic resonance imaging. Magn Reson Med 53:1341-1346.

Summers RM, Hedlund LW, Cofer GP, Gottsman MB, Manibo JF, Johnson GA. 1995. MR microscopy of the rat carotid-artery after balloon injury by using an implanted imaging coil. Magn Reson Med 33:785-789.

Thet LA. 1983. A simple method of intubating rats under direct vision. Lab Anim Sci 33:368-369.

van Beek EJR, Schmiedeskamp J, Wild JM, Paley MNJ, Filbir F, Fichele S, Knitz F, Mills GH, Woodhouse N, Swift A, Heil W, Wolf M, Otten E. 2003. Hyperpolarized 3-helium MR imaging of the lungs: Testing the concept of a central production facility. Eur Radiol 13:2583-2586.

Weissleder R, Mahmood U. 2001. Molecular imaging. Radiology 219:316-333.

Winter PM, Morawski AM, Caruthers SD, Fuhrhop RW, Zhang HY, Williams TA, Allen JS, Lacy EK, Robertson JD, Lanza GM, Wickline SA. 2003. Molecular imaging of angiogenesis in early-stage atherosclerosis with alpha(v)beta(3)-Integrin-targeted nanoparticles. Circulation 108: 2270-2274.

Wixson SK, Smiler KL. 1997. Anesthesia and analgesia in rodents. In: Kohn DF, ed. Anesthesia and Analgesia in Laboratory Animals, Chapter 9. San Diego: Academic Press.

Zhao M, Beauregard DA, Loizou L, Davletov B, Brindle KM. 2001. Non-invasive detection of apoptosis using magnetic resonance imaging and a targeted contrast agent. Nat Med 7:1241-1244.

Zhou YQ, Davidson L, Henkelman RM, Nieman BJ, Foster FS, Yu LX, Chen XJ. 2004. Ultrasound-guided left-ventricular catheterization: A novel method of whole mouse perfusion for microimaging. Lab Invest 84:385-389.